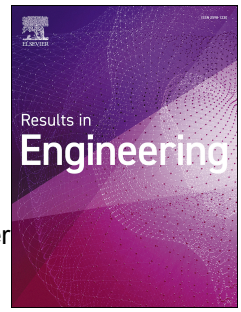

Engineering approach for determining the mechanical behavior of thin welds

Zahra Silvayeh, Josef Domitner, Marius Müller, Peter Auer, Christof Sommitsch, Peter Mayr

PII: S2590-1230(24)00052-5

DOI: https://doi.org/10.1016/j.rineng.2024.101799

Reference: RINENG 101799

To appear in: *Results in Engineering*

Received Date: 11 November 2023

Revised Date: 25 December 2023

Accepted Date: 12 January 2024

Please cite this article as: Z. Silvayeh, J. Domitner, M. Müller, P. Auer, C. Sommitsch, P. Mayr, Engineering approach for determining the mechanical behavior of thin welds, *Results in Engineering* (2024), doi: https://doi.org/10.1016/j.rineng.2024.101799.

Engineering approach for determining the mechanical behavior of thin welds

Zahra Silvayeh[1*], Josef Domitner[1], Marius Müller[1], Peter Auer[1], Christof Sommitsch[1], Peter Mayr[2]

[1] Graz University of Technology (TUG), Institute of Materials Science, Joining and Forming, Research Group of Lightweight and Forming Technologies, Inffeldgasse 11/I, 8010 Graz, Austria

[2] Technical University of Munich (TUM), Chair of Materials Engineering of Additive Manufacturing, Boltzmannstraße 15, 85748 Garching/Munich, Germany

[*]Corresponding author: zahra.silvayeh@tugraz.at

Abstract

Structural components made of thin tailor-welded blanks (TWB) are essential for the design of modern lightweight car bodies. Investigating the formability of these blanks requires detailed information about the mechanical behavior of the weld. Therefore, this study presents an engineering approach that combines experimental and numerical methods for determining elastoplastic properties and fracture parameters of thin aluminum alloy welds produced by gas metal arc (GMA) welding. This approach considers the entire weld seam including surface features as well as inhomogeneous grain structures in as-welded condition, as these features may considerably influence the actual mechanical behavior. Single-pass welds of aluminum alloys AA-5087 and AA-5554 were deposited on a 1.2 mm-thick sheet of aluminum alloy EN AW-5182 using the Cold Metal Transfer (CMT) welding process. Tensile samples consisting almost exclusively of the weld metal were prepared. The three-dimensional (3D) geometries of these samples were captured using an optical scanner. Initial flow curves describing the plastic deformation behavior of the weld were calculated based on the force-elongation curves obtained from tensile testing of the samples. These flow curves and the meshed 3D geometries of the welds were employed for building numerical models of the tensile testing procedure. Flow curves and fracture locus were iteratively optimized until the force-elongation curves calculated in the simulations and measured in the tensile tests matched each other. The elastoplastic properties and the fracture parameters of the aluminum welds can be applied for modeling the weld in deep drawing simulations of tailor-welded blanks consisting of, e.g., different aluminum alloys and steels.

Keywords: Aluminum weld; Fracture behavior; Mechanical properties; Tensile testing; Finite element simulation; Cold Metal Transfer welding (CMT), Tailor-welded blank (TWB);

1. Introduction

The increasing trend towards replacing conventional steels by different materials of higher specific strength and stiffness (e.g., by advanced high-strength steels or aluminum alloys [1,2]) promotes the use of tailor-welded blanks (TWB) for lightweight car body components [3-5]. Multi-material TWB consisting of aluminum alloy sheets and steel sheets with optimized thicknesses can effectively reduce the weight of the car body-in-white (BIW). In general, butt welds are preferred over lap welds for producing thin aluminum-steel TWB that are deep-drawn after the joining process. From the multitude of different thermal joining technologies [6,7], friction stir welding (FSW) [8,9], laser welding-brazing [10,11], Cold Metal Transfer (CMT) gas metal arc (GMA) welding-brazing [12,13], and hybrid arc-laser welding-brazing [14,15] have emerged as suitable for aluminum-steel butt welding. Because of its unique process characteristics featuring controlled metal deposition at low heat input, high efficiency and great flexibility, in particular the CMT technology is very useful for many applications in modern lightweight manufacturing. Potential applications include not only joining [16], but also wire arc additive manufacturing (WAAM) [17-19] of similar and dissimilar metals.

In recent decades, finite element (FE) simulations have increasingly been employed for analyzing deep drawing of TWB [20-24]. However, building reliable numerical models is quite challenging, as the mechanical properties of the weld are often very different to those of the base sheets. The coarse-grained microstructure of the weld has usually lower strength and less ductility than the fine-grained microstructure of the base sheets [5]. Pores inside the weld may also deteriorate the ductility [25-27]. Moreover, thermally-induced resolutionizing and overaging decrease the strength of the HAZ of heat-treatable aluminum alloys (e.g., AA-6xxx), whereas softening of the HAZ of non-heat treatable alloys (e.g., AA-5xxx) is less notable. Hardness measurements can be used for a quick estimation of the local strength. Hardness profiles and maps captured at cross-sections of CMT butt-joined aluminum-steel TWB confirmed, that the hardness decreases within the HAZ of a heat-treatable aluminum alloy sheet, but it increases within the HAZ of the low-alloyed steel sheet [28].

Uniaxial tensile testing has widely been employed for investigating the strength and the ductility of TWB. In this regard, one has to distinguish between testing (i) the overall mechanical properties of the joint or (ii) the specific mechanical properties of the weld [24]. In order to test the properties of the joint, the samples must include both the weld but also the base sheets. Thus, bone-shaped samples of standard size are used, e.g., according to DIN 50125 [29], ISO 6892-1 [30] or ASTM E8/E8M [31], where the weld is aligned perpendicular to the tension direction. Nevertheless, one must consider that the tensile properties are influenced by both the sample size and the fracture mode. For example, the yield strength of friction stir- and laser-welded aluminum alloy AA-6082 TWB was identified to increase with increasing sample size, as the influence of the weld zone decreases [32]. The ductility of CMT-welded-brazed aluminum-steel TWB was found to depend on the location of fracture, which occured either outside the hardened HAZ of the steel sheet, or inside the softened HAZ of the aluminum alloy sheet, or directly at the aluminum-based weld representing the most brittle fracture mode [28]. The fracture mode is mainly influenced by the thickness of the intermetallic layer between the steel sheet and the weld, which can be measured using micrographs of the joint [33] or estimated using numerical simulations of the joining process [34].

In order to determine the specific properties of the weld, the samples must solely consist of the weld metal. Thus, miniature tensile samples smaller than the standard size must be extracted from the welds to exclude any influence of the base sheets in steel TWB [35-38] or aluminum alloy TWB [25-27,39]. Alternatively, researchers tested tensile samples of different size including the base sheets and the weld aligned parallel to the tension direction. Based on these tests they calculated the mechanical properties of the weld of steel TWB using the rule of mixture (ROM) method [40-43]. However, using tensile samples smaller than the standard size is recommended, as standard samples including portions of the base sheets may overestimate the ductility of welds containing pores [26]. Determining the actual cross-section area of the weld is also challenging when using the ROM method [41]. Standard methods for mechanical testing of welds and welded joints are described in AWS B4.0:2016 [44]. These methods feature samples with well-defined geometries (e.g., bone-shaped tensile samples with cylindrical or rectangular cross-sections) that are extracted from the structure or weld to be tested.

In TWB the mechanical properties of the base sheets are usually very different to those of the weld. Hence, testing exclusively the weld metal without any influence of the sheet metal is of utmost importance. This especially applies to TWB consisting of dissimilar materials. Moreover, using representative samples with cross-section dimensions that are quite similar to those of the actual weld is crucial. If the microstructure is non-uniform or if the surface conditions (topography, roughness, etc.) play a significant role, using only a partial volume of the weld metal may affect the testing results. Different cooling and solidification conditions may lead to different microstructures at the weld center, at the weld surface and at the transition zone between the weld and the base sheets, which especially applies to GMA welds. For these reasons, the practicable engineering approach presented in this study considers the entire cross-section of thin aluminum alloy welds. Experimental and numerical methods are combined for determining deformation properties and fracture parameters that are required, e.g., as input for simulating deep drawing of TWB.

2. Experimental methods

As schematically illustrated in Figure 1, the experimental procedure includes (a) single-pass welding, (b) preparation of samples consisting exclusively of the weld metal by milling, (c) digitalization of the three-dimensional (3D) weld geometry using an optical scanner, and (d) uniaxial tensile testing of the samples.

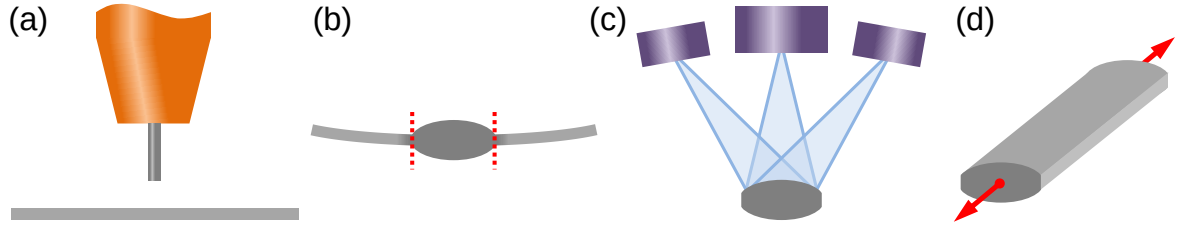

Figure 1: Schematic illustration of the experimental procedure; (a) single-pass welding, (b) preparing/milling the samples, (c) scanning the sample surface and digitalization of the 3D weld geometry, and (d) tensile testing of the samples.

2.1 Welding

Single-pass welds of aluminum alloys AA-5087 and AA-5554 were deposited on a 1.2 mm-thick sheet of aluminum alloy EN AW-5182 using a Fronius CMT Advanced power source. Table 1 contains the nominal chemical compositions of the filler wires and of the base sheet. Partial clamping enabled temperature-induced deformation during the welding process to reduce residual stresses inside the welds. Argon with the flow rate of 12 l/min was used as shielding gas. The mean welding current was 70 A, the mean welding voltage was 8.1 V and the welding speed was 0.4 m/min. Therefore, the nominal heat input was 85 J/mm. The diameter of the filler wires was 1.2 mm and the wire feeding rate was 3.9 m/min. Process parameters, filler wires and the base sheet used in this study were intended for the production of automotive components.

Table 1: Nominal chemical compositions (wt%) of the filler wires and of the base sheet.

Type	Aluminum alloy	Mg	Mn	Si	Fe	Cu	Zn	Ti	Cr	Zr	Al
Filler wire	AA-5087 (Al-4.5Mg-Mn-Zr)	4.5–5.2	0.7–1.1	max. 0.25	max. 0.4	max. 0.05	max. 0.25	max. 0.15	0.05–0.25	0.1–0.2	bal.
Filler wire	AA-5554 (Al-2.7Mg-Mn)	2.4–3.0	0.5–1.0	max. 0.25	max. 0.4	max. 0.1	max. 0.25	0.05–0.2	0.05–0.2	–	bal.
Base sheet	EN AW-5182 (Al-4.5Mg-Mn)	4.0–5.0	0.2–0.5	max. 0.2	max. 0.35	max. 0.15	max. 0.25	max. 0.1	max. 0.1	–	bal.

2.2 Sample preparation

After depositing the weld onto the base sheet, bone-shaped tensile samples as shown in Figure 2 were milled. Note that permanent water cooling of the material during the milling process is crucial to avoid any undesired heating that may affect the microstructure. Optionally, wire cutting with the material placed in a bath of deionized water can be used for manufacturing the samples without significant heat input. The dimensions of the samples were based on DIN 50125, type H. However, the gauge width b was just 5 mm to ensure that the gauge zone consisted almost exclusively of weld metal. The total length L_t of the sample was about 170 mm. The initial gauge length L_0 in tension direction between two reference points on the sample surface was 50 mm. A pattern consisting of randomly distributed black speckles on a white primer was airbrushed onto each sample surface for enabling optical strain measurement during tensile testing. Small spacing platelets were glued onto both ends of each sample to compensate for the thickness of the weld when clamping the samples for tensile testing.

Figure 2: Tensile samples consisting almost exclusively of weld metals AA-5087 and AA-5554, shown after tensile testing.

2.3 Geometry scanning

Before tensile testing, the geometry of each sample was captured contactless using a GOM ATOS Triple Scan (GOM GmbH, Braunschweig, Germany) optical scanner. The data including coordinates of triangles that define the weld surface were stored as *.stl-file. This file format enables transfer and further treatment of the data in the meshing software. Note that exact and careful scanning of the weld surface is essential for capturing all relevant surface features and for simplifying data processing.

2.4 Tensile testing

Figure 3 (a) shows the tensile testing setup. Tensile force-elongation curves were determined at the constant testing speed of 5 mm/min using a Zwick/Roell Z100 (ZwickRoell GmbH & Co. KG, Ulm, Germany) uniaxial testing machine. The GOM ARAMIS (GOM GmbH, Braunschweig, Germany) optical measuring and digital image correlation (DIC) system was used to record the elongation and the strain distribution on the weld surface during testing. The elongation in tension direction was measured between two predefined reference points on the sample surface. The force-elongation curves of several tensile tests showed just moderate differences in the fracture elongation. Therefore, only one force-elongation curve of welds of aluminum alloys AA-5087 and AA-5554, respectively, was considered for FE modeling of the tensile testing procedure.

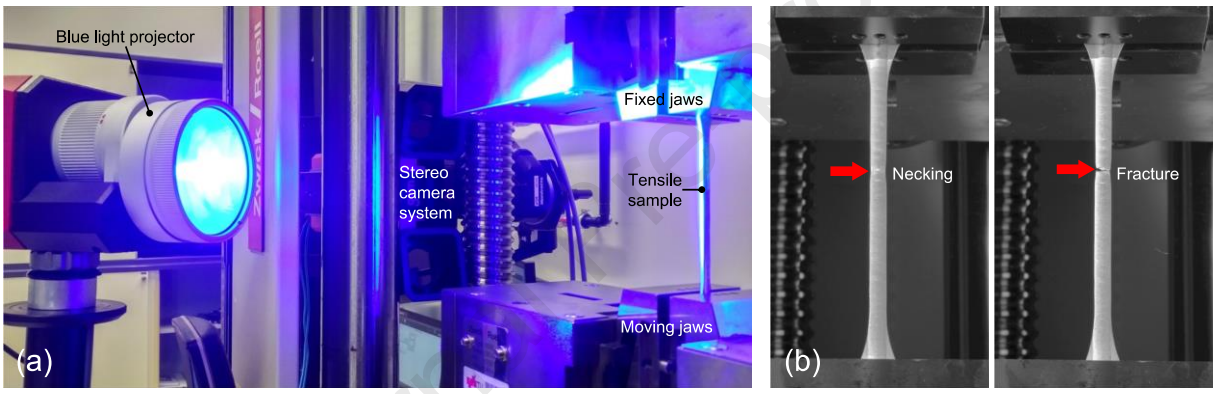

Figure 3: Tensile testing setup (a) and tensile sample (b) shortly before and immediately after final fracture.

2.5 Microstructure investigation

For analyzing the microstructure at the cross-section of each weld, samples were extracted from the broken tensile samples. The samples were cold-embedding into acrylic resin, and their cross-sections were ground, polished and electrolytically etched using Barker's reagent. Micrographs of the cross-sections were finally captured using an Axio Observer.Z1m (Carl Zeiss AG, Jena, Germany) optical microscope equipped with a Zeiss Axio-Cam MRc5 camera and with polarization filters.

3. Numerical methods

Numerical modeling of the tensile testing procedure enabled determining (i) the specific flow curves that characterize the plastic deformation behavior and (ii) the fracture locus that describes the fracture behavior of the weld metal. Therefore, the flow curves and fracture constants that had initially been estimated from the results of the tensile tests were iteratively adjusted, until deformation and fracture behavior of the samples determined in the FE simulations and observed in the tensile tests matched each other. This match was obviously achieved, when the calculated and the measured force-elongation curves were virtually identical.

3.1 Modeling the deformation behavior

For each weld metal an initial flow curve describing the dependency of the flow stress σ from the plastic strain φ was determined. Therefore, the tensile force F_i (N) and the elongation of the sample L_i (mm) were measured during tensile testing at each time increment i. σ_i (N/mm^2) and φ_i (–) were calculated at each of these increments between initial yielding and the onset of local necking:

$$\sigma_i = \frac{F_i L_i}{A_0 L_0} \tag{1}$$

$$\varphi_i = \ln \frac{L_i}{L_0} - \frac{\sigma_i}{E} \tag{2}$$

In Eqs. (1) and (2), the initial gauge length L_0 of the samples was 50 mm and the Young's modulus E of the aluminum alloys was 70×10^3 N/mm^2. The Poisson's ratio was 0.34. The volume V_0 of the deposited weld metal was determined within L_0 based on the 3D digitalization of the samples. The average cross-section area of each weld was then calculated as $A_0 = V_0 / L_0$. Accordingly, A_0 was 666 mm^2 and 688 mm^2 for welds of aluminum alloys AA-5087 and AA-5554, respectively. The well-known Hockett-Sherby relationship [45] was used to fit σ between initial yielding and the onset of necking of the sample and to extrapolate σ beyond necking:

$$\sigma = B - (B - A)\exp(-m\varphi^n) \tag{3}$$

In Eq. (3), the constants A, B, m and n were iteratively adjusted to optimize the initial flow curve in the numerical model until the calculated and the measured force-elongation curves became virtually identical. Moreover, the locations of fracture and the strain fields on the surface of each weld were compared between simulations and experiments.

3.2 Modeling the fracture behavior

According to classical continuum damage mechanics, ductile damage of materials is associated with the nucleation and the growth of microvoids. Coalescence of these voids generates microcracks that reduce the load-bearing capacity and that ultimately cause final fracture of the material [46]. Hence, in order to model ductile damage of the weld, one has to define criteria (i) for fracture initiation as well as (ii) for damage evolution until final fracture.

In principle, any of the numerous fracture models developed for ductile materials can be employed for defining the initiation of fracture. In this work the equivalent plastic strain at fracture initiation, $\bar{\varphi}_f$, was defined based on the criterion introduced by Cockcroft and Latham [47] and modified by Oh et al. [48]. This so-called normalized Cockcroft-Latham or Cockcroft-Latham-Oh criterion assumes that ductile damage and fracture occur, if at least one principal stress component is positive [49], which typically applies to welds during deep drawing of TWB. Bai and Wierzbicki [50] expressed this criterion by introducing the stress triaxiality η and the Lode angle parameter that is also referred to as normalized Lode angle $\bar{\theta}$:

$$\bar{\varphi}_f = C\left(\eta + \frac{2}{3}\cos\left(\frac{\pi}{6}(1-\bar{\theta})\right)\right)^{-1} \tag{4}$$

$\bar{\theta}$ is in the range of $-1 \le \bar{\theta} \le 1$. Eq. (4) demonstrates the main benefit of the normalized Cockcroft-Latham criterion, as only one material-dependent constant C must be determined for defining the fracture locus in the $\eta - \bar{\theta} - \bar{\varphi}_f$ space. In uniaxial straining of smooth round tensile samples with circular cross-section, $\eta = 1/3$ and $\bar{\theta} = 1$; however, both parameters may considerably vary over the cross-section once necking and damage of the material occur [51,52]. Moreover, notches on the surface of round samples significantly influence η. The smaller the notch radius, the greater is η even at the center of the sample [52,53]. Accordingly, the dependency of $\bar{\varphi}_f$ from η cannot be ignored for typical GMA welds having uneven surfaces. Eq. (4) simplifies to Eq. (5), if the cross-section of a thin weld is considered as approximately circular and thus $\bar{\theta} \approx 1$:

$$\bar{\varphi}_f = C(\eta + 2/3)^{-1} \tag{5}$$

In the numerical model the fracture strain $\bar{\varphi}_f$ was defined as function of the stress triaxiality η, as given in Eq. (5). The initial guess of the constant C was iteratively adjusted, until the macroscopic

fracture initiation was virtually identical in both the simulations and the experiments, as indicated by the matching tensile force-elongation curves beyond the force maximum.
In order to model damage evolution until final fracture of the welds, linear softening of the weld metal was supposed, as a steep decline of the force-elongation curves was observed in the tensile tests. Therefore, the equivalent plastic displacement at failure, $\bar{u}_f$, was iteratively determined. $\bar{u}_f$ considers (i) the difference between the equivalent plastic strains at final fracture and at fracture initiation, as well as (ii) the characteristic element length [54]. Final fracture of the welds was supposed to occur when the material stiffness degraded by 99 %.

3.3 Mesh and boundary conditions

The digitalized 3D geometries of the welds were pre-processed for finite element analysis using the HyperMesh (Altair Engineering, Inc., Troy, MI, Unites States) software. Pre-processing included restoring the measured sample surfaces and meshing the sample volume enclosed by these surfaces. The meshed geometries were then imported into the Abaqus FEA 2017 software package (Dassault Systèmes SE, Vélizy-Villacoublay, France). Figure 4 exemplarily shows the model of the tensile sample consisting of aluminum alloy AA-5087. Because of the fine mesh, all relevant surface features of the weld were well represented. Unstructured volume meshes featuring 4-node linear tetrahedron elements of type C3D4 were used at both ends (blue), whereas a structured volume mesh featuring 8-node linear hexahedral brick elements of type C3D8 was used at the central part of the sample (green). The nodes at one end of the sample were fixed. The nodes at the other end were displaced parallel to the x-axis of the sample by 12 mm within 144 s, i.e., they were displaced with the constant velocity of 5 mm/min as in the tensile tests. The reaction forces at the moving nodes were integrated in tension direction to determine the total tensile force, and the displacement of two selected nodes on the weld surface was monitored to determine the elongation of the sample. The initial distance between both surface nodes was 50 mm, which was equal to the initial gauge length in the tensile tests. The FE simulation was performed using the Abaqus/Standard solver for general nonlinear dynamic analysis with implicit time integration.

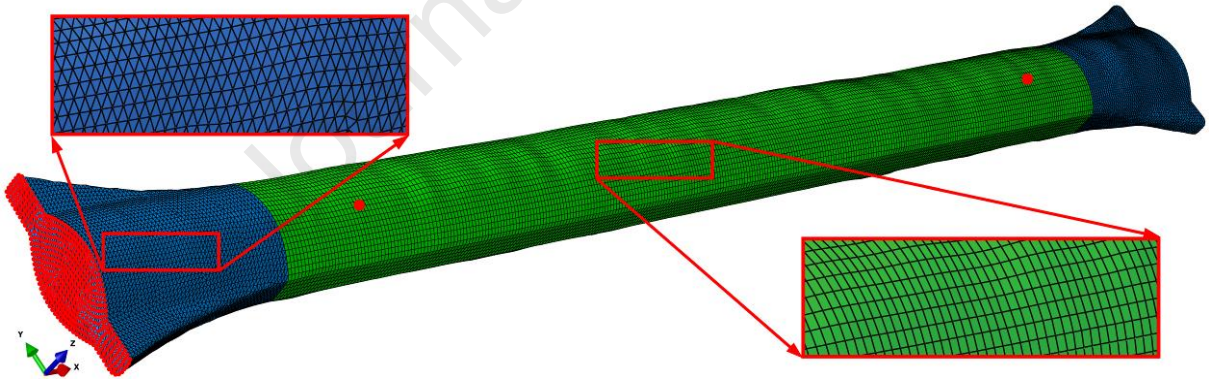

Figure 4: Meshed model of the tensile sample of aluminum alloy AA-5087 consisting of tetrahedron (blue) and brick (green) elements. The nodes at the left end of the sample (red) were fixed. The displacement of the two nodes on the weld surface (red) was monitored for determining the elongation of the sample.

4. Results and discussion

4.1 Microstructure

Figure 5 shows microstructures of welds consisting of aluminum alloys AA-5087 (a) and AA-5554 (b). Welds with comparable microstructures were also achieved in Cold Metal Transfer (CMT) butt welding-brazing of 1.2 mm-thick aluminum alloy sheets with 0.8 mm-thick steel sheets [13,28,33,34]. The difference between the coarse-grained globular microstructure of the aluminum alloy welds and the fine-grained globular microstructure of the aluminum alloy sheets at both sides of the welds is evident. Moreover, columnar grains are visible at the transition zones next to the sheets. Note that the determined elastoplastic properties of the weld metal are only reliable, if the area fraction of the fine globular grains is negligible.

As given in Table 1, the magnesium content of aluminum alloy AA-5087 is about two-times higher than the magnesium content of aluminum alloy AA-5554, whereas the contents of other alloying elements are quite similar. As the solidification interval expands with increasing magnesium content [55], the microstructure shown in Figure 5 (a) is coarser than the microstructure shown in Figure 5 (b), although the welding parameters and cooling conditions were de facto identical.

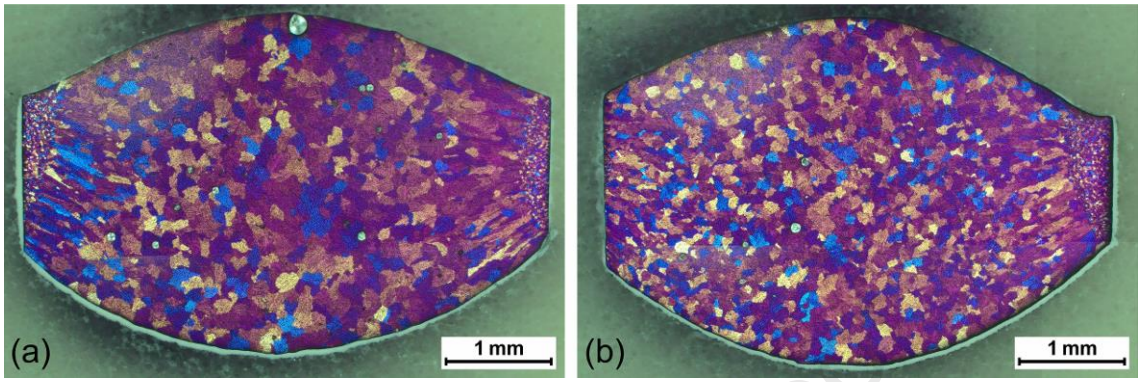

Figure 5: Typical microstructures of welds of aluminum alloys AA-5087 (a) and AA-5554 (b).

4.2 Flow curves and fracture behavior

Table 2 summarizes iteratively determined parameters that define the flow curves (A, B, m and n) and the fracture behavior (C and $\bar{u}_f$) of welds of aluminum alloys AA-5087 and AA-5554. A and B are different, but m, n, C and $\bar{u}_f$ are identical for both welds.

Table 2: Parameters defining the flow curves and the fracture behavior of the welds.

Aluminum alloy	A	B	m	n	C	$\bar{u}_f$
AA-5087 (Al-4.5Mg-Mn-Zr)	135 N/mm^2	395 N/mm^2	5	¾	¼	0.1 mm
AA-5554 (Al-2.7Mg-Mn)	110 N/mm^2	340 N/mm^2	5	¾	¼	0.1 mm

The full lines in Figure 6 represent stress-strain curves (a) and flow curves (b) that were deduced from the force-elongation curves determined by uniaxial tensile testing. Based on these curves, the dashed flow curves illustrated in Figure 6 (b) were calculated in the iterative modeling process. Because local necking of the samples and thus local multi-axial straining occurred in tensile testing, the flow curves were extrapolated beyond the true strain of $\varphi \approx 0.13$. It is evident that the flow stress σ of the weld of aluminum alloy AA-5087 was higher than the flow stress of the weld of aluminum alloy AA-5554. This is likely due to the higher magnesium content that enhances solid solution strengthening of AA-5087 compared to AA-5554 [56], although the finer grains of AA-5554 may basically promote Hall-Petch strengthening [57,58].

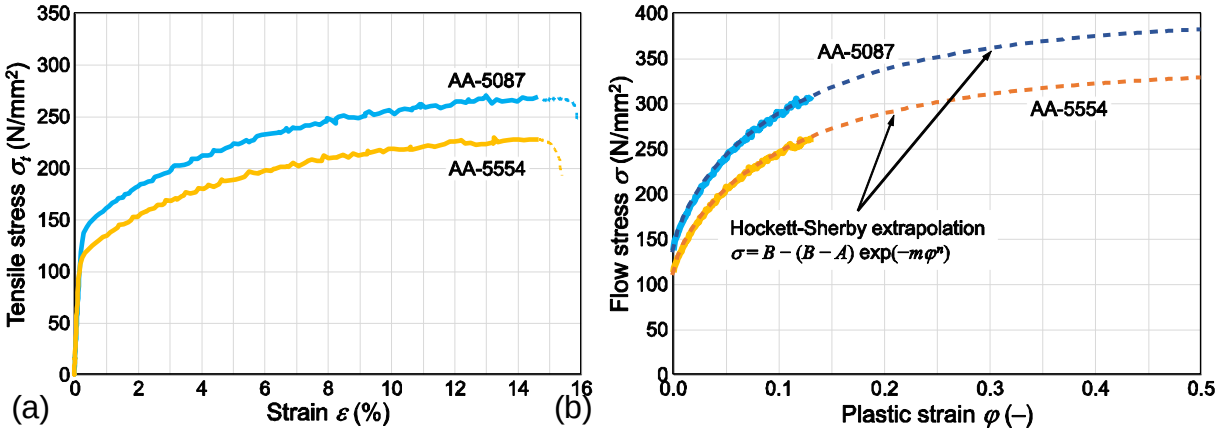

Figure 6: Measured stress-strain curves (a) and extrapolated flow curves (b) of aluminum alloys AA-5087 and AA-5554.

The fracture locus according to the normalized Cockcroft-Latham fracture criterion was defined for both aluminum alloys in the $\eta - \bar{\theta} - \bar{\varphi}_f$ space, as illustrated in Figure 7. It is evident that $\bar{\varphi}_f$ strongly depends on the stress triaxiality η, but just moderately on the Lode angle parameter $\bar{\theta}$. If η is positive, $\bar{\varphi}_f$ is comparatively small; however, if η becomes negative, $\bar{\varphi}_f$ strongly increases. Hence, ductile fracture can be excluded beyond $\eta \approx$ -2/3, because $\bar{\varphi}_f$ becomes infinity. This agrees with practical observations, as particularly tensile stresses but not compressive stresses are most critical with regard to thinning and fracture, especially in deep drawing. Hence, the obtained fracture locus can be considered as feasible for estimating the actual fracture behavior of welds, e.g., in deep drawing simulations of TWB.

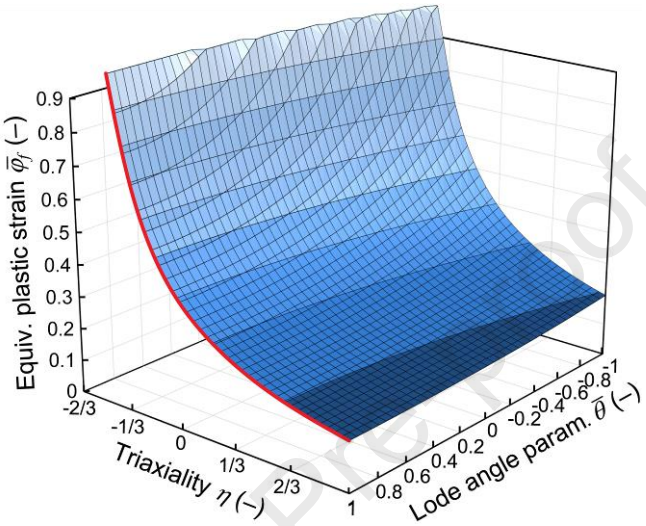

Figure 7: Fracture locus describing the fracture behavior of welds of aluminum alloys AA-5087 and AA-5554. The red curve at $\bar{\theta} = 1$ was determined by adjusting the constant C in Eq. (5) and the blue surface for $-1 \leq \bar{\theta} \leq 1$ was extrapolated using Eq. (4).

4.3 Comparison of simulations and experiments

Figure 8 compares the tensile force-elongation curves that were obtained in the experiments and in the simulations for welds of aluminum alloys AA-5087 and AA-5554. It is evident that macroscopic deformation as well as fracture of the welds was well predicted by the numerical model, as the curves calculated using the parameters given in Table 2 are consistent with the curves determined in the tensile tests. In particular, the steep decline of each curve beyond the tensile force maximum was properly modeled. Note that the fracture elongation can vary, if several tensile samples even of the same weld metal are tested. This variation, which is typical for weld metals containing defects, can be considered in the model by adjusting the parameter C in Eqs. (4) and (5) by about 10 %.

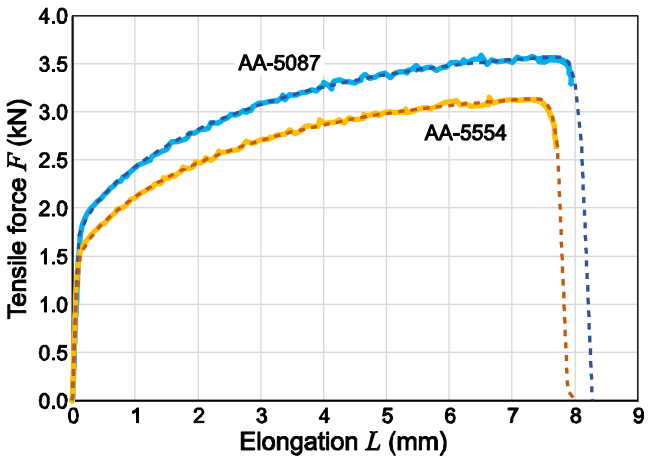

Figure 8: Tensile force-elongation curves of welds of aluminum alloys AA-5087 and AA-5554 obtained from experiments (continuous lines) and simulations (dashed lines).

Figure 9 exemplarily compares the equivalent plastic strain $\overline{\varphi}$ on the surface of the weld consisting of aluminum alloy AA-5087. Directly before and after final fracture of the sample the strain field was calculated in the simulation (a) and measured in the experiment (b). Even outside the necking zone the strain fields in both simulation and experiment were non-uniform, which was due to the uneven surface of the weld. Despite the good general agreement between the numerical and the experimental results (the location of strain concentration was identical), the orientation of the fracture surface was different. This difference was mainly attributed to microscopic defects (e.g., pores or non-metallic inclusions) that were present in the weld, as exemplarily illustrated in Figure 10. Such defects may notably trigger the initiation and growth of local microcracks causing more brittle behavior of the weld. Although the influence of microscopic defects was not explicitly modeled, the model was able to predict the macroscopic response of the weld metal that is affected by the defects, as confirmed by the matching force-elongation curves in Figure 8.

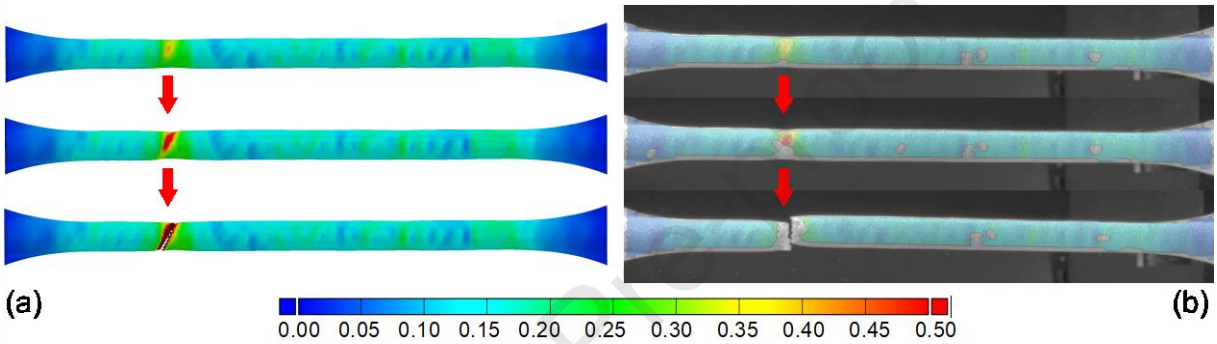

Figure 9: Fracture behavior of the tensile sample of aluminum alloy AA-5087 as calculated in the simulation (a) and measured in the experiment (b). The colors represent the equivalent plastic strain $\overline{\varphi}$ (–) on the as-welded sample surface directly before (top), during (center) and directly after (bottom) final fracture that occurred at the position marked by the red arrows.

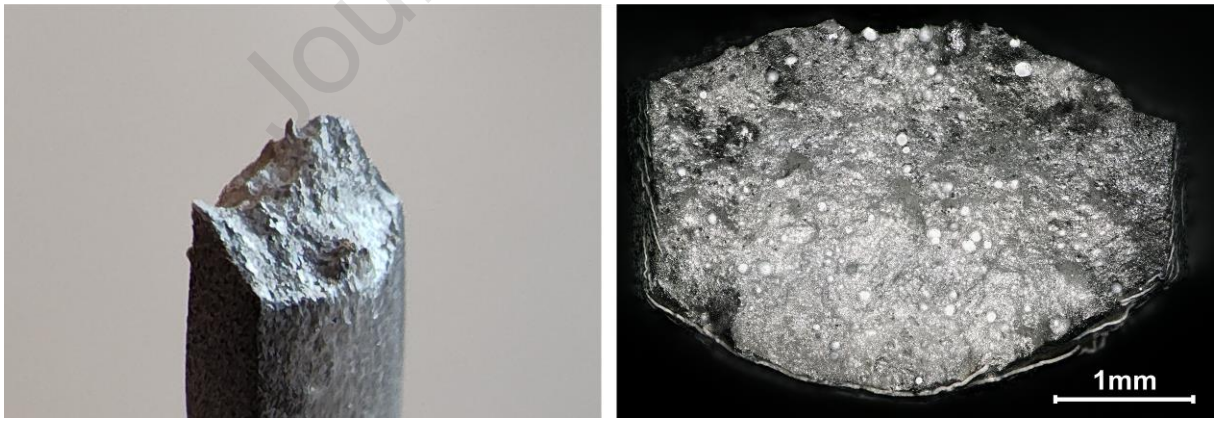

Figure 10: Fracture surface of the tensile sample of aluminum alloy AA-5087. Numerous spherical gas pores (white) and non-metallic inclusions (grey) are visible. As local necking occurred during tensile testing, the area of the projected fracture surface is smaller than the area of the sample cross-section that was only exposed to uniform straining.

Figure 11 demonstrates the evolution of the equivalent plastic strain $\overline{\varphi}$ on the surface of the weld consisting of aluminum alloy AA-5087. Local necking of the sample started at the “sharpest notch” on the uneven weld surface. If the condition $\overline{\varphi} = \overline{\varphi}_f(\eta)$ was fulfilled in a single element, fracture was initiated and damage accumulation continued with increasing plastic displacement. Hence, the load-bearing capacity of this element was continuously degraded. As fully degraded elements were deleted from the mesh, a fracture surface similar to that in the experiment was obtained in the simulation.

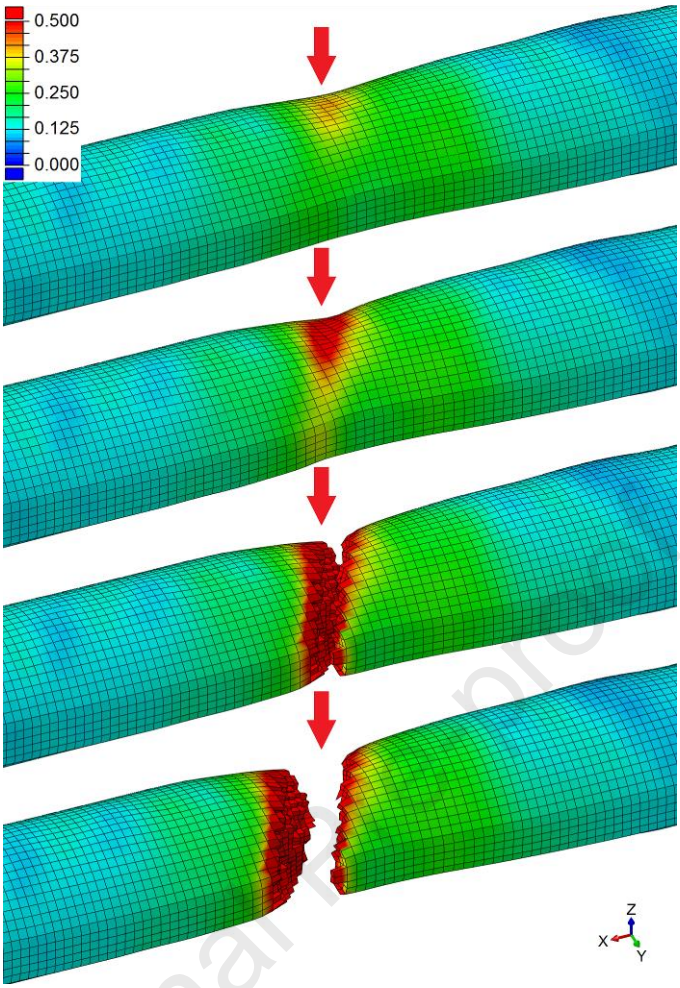

Figure 11: Detail showing local necking and subsequent macroscopic fracture as calculated in the simulation of the tensile sample of aluminum alloy AA-5087. The colors represent the equivalent plastic strain $\overline{\varphi}$ (–), which increases from initial necking until final fracture.

Figure 12 shows the evolution of the equivalent plastic strain $\overline{\varphi}$ (a) and of the triaxiality η (b) at the critical cross-section of the weld, as marked with the red arrow in Figure 11. Before necking η and $\overline{\varphi}$ were virtually constant over the cross-section, and both varied just moderately on the uneven surface. Once necking started, $\overline{\varphi}$ increased firstly on the surface, but due to the emerging multi-axial stress/strain condition η even increased inside the sample. After final macroscopic fracture, the plastic deformation at the fracture surface was still apparent, but the stresses were released and thus η decreased inside the sample. According to the fracture locus illustrated in Figure 7, fracture initiation is expected at the element that has the greatest η and therefore the lowest $\overline{\varphi}_f(\eta)$.

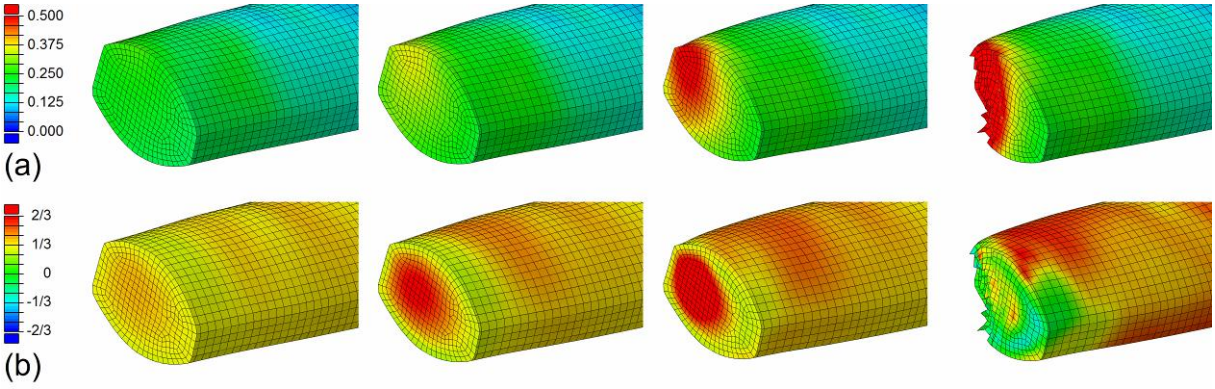

Figure 12: Increase of the (a) equivalent plastic strain $\overline{\varphi}$ (–) and of the (b) triaxiality η (–) at the critical cross-section as calculated in the simulation of the tensile sample of aluminum alloy AA-5087.

5. Conclusions

A practicable engineering approach that includes experimental and numerical methods was presented, which can be used for determining material parameters that characterize the plastic deformation and the fracture behavior of thin welds. The feasibility of this approach was demonstrated for welds of aluminum alloys AA-5087 and AA-5554. Based on the results of this study, the following conclusions can be drawn:

(1) The experimental efforts for the mechanical characterization of the welds are low, as the procedure is solely based on uniaxial tensile testing of samples considering the entire cross-section of the weld. If the tensile sample is properly prepared, the exclusive properties of the weld can be determined without any influence of the base sheets or of the heat-affected zone.

(2) Before tensile testing, an optical scanner is used to capture the three-dimensional sample geometry including all relevant features of the weld surface. During tensile testing, the strain on the weld surface is recorded using an optical measuring and digital image correlation system. As these contactless measurements are not subjected to any dimensional restrictions, length and width of the sample are fully scaleable to the actual dimensions of the weld.

(3) The fracture in deep drawing of tailor-welded blanks is mainly initiated in regions of high tensile stresses, which benefits the use of the normalized Cockcroft-Latham fracture criterion. Moreover, this criterion is easy to calibrate, as the fracture locus can be defined by only a single constant. However, a more sophisticated fracture criterion may better predict fracture initiation at negative triaxiality.

(4) Although the macroscopic deformation and fracture behavior of the welds were basically well described by the numerical model, anisotropic material properties, internal microscopic defects (e.g., pores and non-metallic inclusions) or residual stresses may notably influence the actual properties of the weld. These effects are currently not considered in the model.

(5) Flow curves and fracture parameters of thin welds as determined in the present work can be used for modeling deep drawing of tailor-welded blanks. Nevertheless, in particular finite element models of dissimilar aluminum-steel blanks must also consider the bonding characteristics and the fracture behavior of the intermetallic layer that forms between the aluminum-based weld and the steel sheet. Determining these properties is an ongoing research.

Credit author contribution statement

Zahra Silvayeh: Conceptualization, Methodology, Investigation, Data curation, Visualization, Writing – original draft. Josef Domitner: Conceptualization, Writing – review & editing, Formal analysis, Resources, Project management, Supervision. Marius Müller: Investigation. Peter Auer: Investigation. Christof Sommitsch: Supervision. Peter Mayr: Supervision.

Declaration of competing interest

The authors declare that they have no known competing financial interests or personal relationships that could have appeared to influence the work reported in this paper.

Acknowledgement

Part of this work was co-funded by the Erasmus+ Programme of the European Union. Open access funding was provided by Graz University of Technology.

References

[1] A. Taub, E. De Moor, A. Luo, D.K. Matlock, J.G. Speer, U. Vaidya, Materials for automotive lightweighting, *Annu. Rev. Mater. Res.* 49 (2019) 327–359.

[2] W. Zhang, J. Xu, Advanced lightweight materials for automobiles: A review, *Mater. Des.* 221 (2022) 110994.

[3] B.L. Kinsey, Tailor welded blanks for the automotive industry, in: B.L. Kinsey, X. Wu, ed. *Tailor welded blanks for advanced manufacturing*, Woodhead Publishing, Cambridge, UK, 2011, 164–180.

[4] G.A. Kunkel, Y. Hovanski, From the Lab to Your Driveway: Aluminum Tailor-Welded Blanks, *Weld. J.* 95 (2016) 36–39.

[5] M. Merklein, M. Johannes, M. Lechner, A. Kuppert, A review on tailored blanks – Production, applications and evaluation, *J. Mater. Process. Technol.* 214 (2014) 151–164.

[6] A. Gullino, P. Matteis, F. D'Aiuto, Review of Aluminum-To-Steel Welding Technologies for Car-Body Applications, *Metals* 9 (2019) 315, doi:10.3390/met9030315.

[7] M. Mazar Atabaki, M. Nikodinovski, P. Chenier, J. Ma, M. Harooni, R. Kovacevic, Welding of Aluminum Alloys to Steels: An Overview, *J. Manuf. Sci. Prod.* 14 (2014) 59–78.

[8] M. Merklein, A. Giera, M. Geiger, Deep Drawing of Friction Stir Welded Thin Sheet Aluminium Steel Tailored Hybrids, *Steel Res. Int.* 76 (2005) 250–256.

[9] F. Panzer, M. Schneider, M. Werz, S. Weihe, Friction stir welded and deep drawn multi-material tailor welded blanks, *Mater. Test.* 61 (2019) 643–651.

[10] D. Wallerstein, A. Salminen, F. Lusquiños, R. Comesaña, J. del Val García, A. Riveiro Rodríguez, A. Badaoui, J. Pou, Recent Developments in Laser Welding of Aluminum Alloys to Steel, *Metals* 11 (2021) 622, https://doi.org/10.3390/met11040622.

[11] J. Yang, J.P. Oliveira, Y. Li, C. Tan, C. Gao, Y. Zhao, Z. Yu, Laser techniques for dissimilar joining of aluminum alloys to steels: A critical review, *J. Mater. Process. Technol.* 301 (2022) 117443.

[12] O. Singar, M. Merklein, Study on formability characteristics of the weld seam of aluminum steel tailored hybrid blanks, *Key Eng. Mater.* 549 (2013) 302–310.

[13] B. Götzinger, W. Karner, M. Hartmann, Z. Silvayeh, Optimised process for steel-aluminium welding, *Lightw. Des. Worldw.* 10 (2017) 42–46.

[14] J. Xue, Y. Li, H. Chen, Z. Zhu, Effects of heat input on wettability, interface microstructure and properties of Al/steel butt joint in laser-metal inert-gas hybrid welding-brazing, *J. Mater. Process. Technol.* 255 (2018) 47–54.

[15] S. Chen, S. Li, Y. Li, J. Huang, S. Chen, J. Yang, Butt welding-brazing of steel to aluminum by hybrid laser-CMT, *J. Mater. Process. Technol.* 272 (2019) 163–169.

[16] S. Selvi, A. Vishvaksenan, E. Rajasekar, Cold metal transfer (CMT) technology - An overview, *Def. Technol.* 14 (2018) 28–44.

[17] B. Wu, Z. Pan, D. Ding, D. Cuiuri, H. Li, J. Xu, J. Norrish, A review of the wire arc additive manufacturing of metals: properties, defects and quality improvement, *J. Manuf. Process.* 35 (2018) 127–139.

[18] Y. Li, C. Su, J. Zhu, Comprehensive review of wire arc additive manufacturing: Hardware system, physical process, monitoring, property characterization, application and future prospects, *Results Eng.* 13 (2022) 100330.

[19] C. Yin, J. Shen, S. Hu, Z. Zhang, Microstructure and mechanical properties of AZ91 magnesium alloy fabricated by multi-layer and multi-pass CMT based WAAM technique, *Results Eng.* 18 (2023) 101065.

[20] F.I. Saunders, R.H. Wagoner, Forming of Tailor-Welded Blanks, *Metall. Mater. Trans.* 27A (1996) 2605–2616.

[21] T. Meinders, A. van den Berg, J. Huétink, Deep drawing simulations of Tailored Blanks and experimental verification, *J. Mater. Process. Technol.* 103 (2000) 65–73.

[22] R. Padmanabhan, M.C. Oliveira, L.F. Menezes, Deep drawing of aluminium-steel tailor-welded blanks, *Mater. Des.* 29 (2008) 154–160.

[23] A.A. Zadpoor, J. Sinke, R. Benedictus, Finite element modeling and failure prediction of friction

stir welded blanks, *Mater. Des.* 30 (2009) 1423–1434.
[24] A.A. Zadpoor, J. Sinke, R. Benedictus, Mechanics of Tailor Welded Blanks: An Overview, *Key Eng. Mater.* 344 (2007) 373–382.
[25] R.W. Davies, H.E. Oliver, M.T. Smith, G.J. Grant, Characterizing Al Tailor-Welded Blanks for Automotive Applications, *JOM* 51 (1999) 46–50.
[26] R.W. Davies, M.T. Smith, H.E. Oliver, M.A. Khaleel, S.G. Pitman, Weld Metal Ductility in Aluminum Tailor Welded Blanks, *Metall. Mater. Trans.* 31A (2000) 2755–2763.
[27] G.T. Kridli, P.A. Friedman, A.M. Sherman, Formability of Aluminum Tailor-Welded Blanks, *SAE Tech. Paper Ser.* 01 (2000) 0772.
[28] Z. Silvayeh, J. Domitner, C. Sommitsch, M. Hartmann, W. Karner, B. Götzinger, Mechanical properties and fracture modes of thin butt-joined aluminum-steel blanks for automotive applications, *J. Manuf. Process.* 59 (2020) 456–467.
[29] DIN 50125. Testing of metallic materials – Tensile test pieces, 2016.
[30] ISO 6892-1. Metallic materials – Tensile testing – Part 1: Method of test at room temperature, 2019.
[31] ASTM E8/E8M. Standard test methods for tension testing of metallic materials, 2022.
[32] J. Liu, L.L. Wang, J. Lee, R. Chen, O. El-Fakir, L. Chen, J. Lin, T.A. Dean, Size-dependent mechanical properties in AA6082 tailor welded specimens, *J. Mater. Process. Technol.* 224 (2015) 169–180.
[33] Z. Silvayeh, R. Vallant, C. Sommitsch, B. Götzinger, W. Karner, M. Hartmann, Influence of filler alloy composition and process parameters on the intermetallic layer thickness in single-sided cold metal transfer welding of aluminum-steel blanks, *Metall. Mater. Trans.* 48A (2017) 5376–5386.
[34] Z. Silvayeh, B. Götzinger, W. Karner, M. Hartmann, C. Sommitsch, Calculation of the intermetallic layer thickness in cold metal transfer welding of aluminum to steel, *Materials* 12 (2019) 35, https://doi.org/10.3390/ma12010035.
[35] C.H. Cheng, M. Jie, L.C. Chan, C.L. Chow, True stress-strain analysis on weldment of heterogeneous tailor welded blanks – a novel approach for forming simulation, *Int. J. Mech. Sci.* 49 (2007) 217–229.
[36] M. Abbasi, M. Ketabchi, H.R. Shakeri, M.H. Hasannia, Formability Enhancement of Galvanized IF-Steel TWB by Modification of Forming Parameters, *J. Mater. Eng. Perform.* 21 (2012) 564–571.
[37] M. Abbasi, M. Ketabchi, T. Labudde, U. Prahl, W. Bleck, New attempt to wrinkling behavior analysis of tailor welded blanks during the deep drawing process, *Mater. Des.* 40 (2012) 407–414.
[38] L. Hétu, K. Siegert, Hydromechanical Deep Drawing of Tailor Welded Blanks, *Steel Res. Int.* 76 (2005) 857–865.
[39] R.W. Davies, G.J. Grant, H.E. Oliver, M.A. Khaleel, M.T. Smith, Forming-Limit Diagrams of Aluminum Tailor-Welded Blank Weld Material, *Metall. Mater. Trans.* 32A (2001) 275–283.
[40] B.Y. Ghoo, Y.T. Keum, Y.S. Kim, Evaluation of the mechanical properties of welded metal in tailored steel sheet welded by CO_2 laser, *J. Mater. Process. Technol.* 113 (2001) 692–698.
[41] K. Abdullah, P.M. Wild, J.J. Jeswiet, A. Ghasempoor, Tensile testing for weld deformation properties in similar gage tailor welded blanks using the rule of mixtures, *J. Mater. Process. Technol.* 112 (2001) 91–97.
[42] Y. Song, L. Hua, D. Chu, J. Lan, Characterization of the inhomogeneous constitutive properties of laser welding beams by the micro-Vickers hardness test and the rule of mixture, *Mater. Des.* 37 (2012) 19–27.
[43] Y. Song, L. Hua, Formability of tailor welded blanks based on the improved rule of mixture considering the welding residual strain and stress, *Appl. Mech. Mater.* 152–154 (2012) 1406–1412.
[44] AWS B4.0, Standard Methods for Mechanical Testing of Welds, 8th ed., 2016.
[45] J.E. Hockett, O.D. Sherby, Large strain deformation of polycrystalline metals at low homologous temperatures, *J. Mech. Phys. Solids* 23 (1975) 87–98.
[46] A.E. Tekkaya, P.-O. Bouchard, S. Bruschi, C.C. Tasan, Damage in metal forming, *CIRP Annals*

Manuf. Technol. 69 (2020) 600–623.
[47] M.G. Cockcroft, D.J. Latham, Ductility and the workability of metals, *J. Inst. Metals* 96 (1968) 33–39.
[48] S.I. Oh, C.C. Chen, S. Kobayashi, Ductile fracture in axisymmetric extrusion and drawing – part 2: Workability in extrusion and drawing, *J. Eng. Ind.* 101 (1979) 36–44.
[49] Y. Bai, T. Wierzbicki, A Comparative Study on Various Ductile Crack Formation Criteria, *Trans. ASME* 126 (2004) 314–324.
[50] Y. Bai, T. Wierzbicki, A comparative study of three groups of ductile fracture loci in the 3D space, *Eng. Fract. Mech.* 135 (2015) 147–167.
[51] Y. Bao, T. Wierzbicki, On fracture locus in the equivalent strain and stress triaxiality space, *Int. J. Mech. Sci.* 46 (2004) 81–98.
[52] Y. Bai, X. Teng, T. Wierzbicki, On the Application of Stress Triaxiality Formula for Plane Strain Fracture Testing, *J. Eng. Mater. Technol.* 131 (2009) 021002.
[53] P.W. Bridgman, *Studies in Large Plastic Flow and Fracture*, McGraw-Hill, New York, USA, 1952.
[54] Abaqus Analysis User's Guide Volume III: Materials, Dassault Systèmes SE, Vélizy-Villacoublay, France, 2015.
[55] J.L. Murray, Al-Mg (Aluminum-Magnesium) phase diagram, in: *ASM Handbook, Volume 3: Alloy Phase Diagrams*, ASM International, Materials Park, OH, 1988.
[56] G. Mathers, *The welding of aluminium and its alloys*, Woodhead Publishing, Cambridge, UK, 2002.
[57] E.O. Hall, The deformation and ageing of mild steel: III discussion of results, *Proc. Phys. Soc. B* 64 (1951) 747–753.
[58] N.J. Petch, The cleavage strength of polycrystals, *J. Iron Steel Inst.* 174 (1953) 25–28.

Highlights

- The presented engineering approach combines experimental and numerical methods.
- Macroscopic deformation and fracture behavior of aluminum welds are determined.
- The entire weld seam with as-welded surface and microstructure is considered.
- Well-established plasticity and fracture models are employed.
- The results can be used for simulating deep drawing of tailor welded blanks.

Declaration of interests

X The authors declare that they have no known competing financial interests or personal relationships that could have appeared to influence the work reported in this paper.

☐The authors declare the following financial interests/personal relationships which may be considered as potential competing interests: